Acta Microscopica Vol. 29, No.1, 2020, pp.87-97

Environmental Adaptation of a Lightweight Design Airborne Spectroscopic Imager

Siyu Wang
Academy of Opto-electronics, Chinese Academy of Sciences, Beijing 100091, China
University of Chinese Academy of Sciences, Beijing 100049, China

Min Huang*
Academy of Opto-electronics, Chinese Academy of Sciences, Beijing 100091, China
University of Chinese Academy of Sciences, Beijing 100049, China
**Corresponding author*

Changxiang Yan
Changchun Institute of Optics, Fine Mechanics and Physics, Chinese Academy of Sciences, Changchun 100033, China
University of Chinese Academy of Sciences, Beijing 100049, China

Abstract
This paper details the design of a light airborne imaging spectrometer in order to improve real-time monitoring of natural disasters. This deisgn is based on a lightweight concept, and focuses on the adaptability of the spectrometer in varied environments. First, the optomechanical support structure of the spectrometer were designed by using filter spectrometry, push-broom imaging method and topology optimization, based on the design principles of optimal optical parameters and light weight. Next, a finite element model of the structure was used to analyze the linear static structure, the natural vibrational characteristics, the strength, the optical lens deformation and the modal frequency. Finally, the spectrometer was tested for surface accuracy detection via field experiments. The experimental results show that the ground phase element resolution of the spectrometer is $0.5\,m/km$, the size is $175\times 175\times 175\,mm$, and the machine structure weight is $1.15\,kg$. The optical machine structure strength and the deformation of the optical lens exceed the target requirements, with a first order modal frequency of $590.8\,Hz$. The drone can maintain good performance in the temperature range of 0~40$^{\circ}C$ with wind conditions less than or equal to 7 and a cruising speed of $100\,km/h$.

Key words: Airborne Instrumentation, Imaging Spectrometer, Lightweight Construction, Environmental adaptation.

1. Introduction

The main goal of lightweight-designed airborne spectrometer imaging is the acquisition of fast, accurate and stable dynamic information about natural disasters, public safety and social services. For example, a drone can fly into a disaster area before emergency services on the ground can respond, especially if roads are inaccessible. An imaging spectrometer and other related instruments can obtain real-time monitoring data in multiple dimensions, quickly realize disaster assessment for rescue, and provide valuable guidance for emergency service response [1,2]. In addition, it can be combined with other airborne imaging and radar systems to enable multi-source information networking and big data collaboration.

Developed countries have been conducting research on imaging spectrometers since the 1980s. For example, AVIRIS in the United States and HyMap in Australia are typical spectral imagers, which both use push-pull imaging. The spectral range of AVIRIS is 400-2500$\,nm$, with a field of view of 30° and a weight of $39\,kg$. The spectral range of HyMap is also 400-2500$\,nm$, with a field of view of 60° and a weight of about 200 kg [3,4]. The rapid development of drones has yielded a greater advantage over general-purpose aircraft in the field of natural disaster monitoring, which can save cost and increase maneuverability, as well as having the ability to adapt to complex environments and has lessen safety risks [5]. For example, the latest research on the HySpex Mjolnir imaging spectrometer based out of Norway ($4\,kg$ weight, $250\times 170\times 170\,mm$ size) uses a convex grating to split light and can be placed on a fixed-wing UAV platform as a separate module [6-7]. In recent years, China has carried out in-depth research about imaging spectrometers and achieved a series of results. Some of these milestones are Congjun Wu and others at the Changchun Institute of Optics and Fine Mechanics, Chinese Academy of Sciences, who designed a prism-grating based spectral spectroscopic system [8]. Gangyin Luo and others from the Suzhou Medical Institute at the Chinese Academy of Sciences also conducted related experiments on this type of spectroscopic system [9]. Zhiliang Gao of the Changchun Institute

of Optics and Fine Mechanics, Chinese Academy of Sciences, also designed an equivalent focal plane adjustment module for hyperspectral imagers [10]. Min Huang and others from the Beijing Institute of Optoelectronics, Chinese Academy of Sciences, proposed an effective data inversion method and process for spatially modulated interference spectral imagers [11]. Research in China is progressing rapidly in this field, however, end products of light UAV-borne imaging spectrometers with independent intellectual property rights are still lacking. This paper will focus on the research of lightweight platforms with effective environmentally adaptative imaging spectrometer system, with an ancillary focus on the issues of unmanned space, load capacity, and endurance.

2. Theory and Process

2.1. Spectrometer Theory

The components of an imaging spectrometer are an optical system, an aperture, a focal plane component, a control system, and an electronic system. The spectrometer will be mounted on a lightweight drone that also carries several imaging and radar systems. The workflow of the imaging spectrometer is shown in Figure. 1.

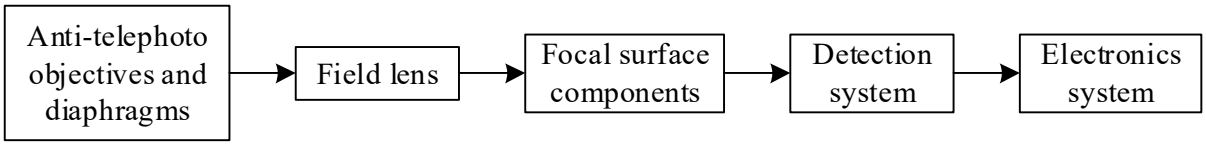

Figure 1. Conceptual workflow and theory of the operation of an imaging spectrometer.

In the operation of an imaging spectrometer, light first enters the anti-telephoto objective and the aperture stop. Next, the field lens in front of the focal plane forms an image-side telecentric focal plane component to split the light. Finally, the detection system performs imaging and detection, and the electronics system performs data processing and transmission.

2.2. Detection Process

The spectrometer's instantaneous field of view iFie, flight speed v, flight altitude H, and integration time T have the following relation,

$$T = iF_{ie}\frac{H}{v} \tag{1}$$

The detection process is shown in Figure. 2. In the spatial dimension, when the aircraft is flying, the wide field of view telescope performs a one-dimensional scan perpendicular to the flight direction, and the movement of the flight platform along the flight direction performs another one-dimension scan. In the spectral dimension, the telescope system images the light from the ground object onto the incident slit of the spectrometer, which helps to achieve information acquisition over large areas. The light enters the spectroscopic system through the slit, and the entire wavelength band is divided into several sub-bands by the spectroscopic element, which is then imaged on the linear array detector. The target's spectral information is unfolded one-dimensionally on the detector to achieve the spectral information of the object.

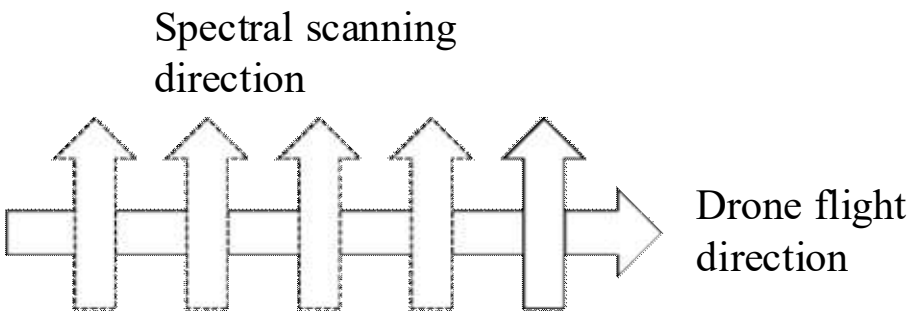

Figure 2. Detection process of an imaging spectrometer.

Finally, data cubes containing the spatial and spectral dimensional information of the features can be obtained.

3. Design and Analysis

3.1. Optical Design

Optimal imaging spectrometers have a field angle of $60°$, and a spectral imaging range of 400 to $1000\,nm$. With these specifications, a target can be identified at $0.5\,m$ resolution from a height of $1\,km$. Additionally, the weight of the optical-mechanical structure should not exceed $1.5\,kg$. In accordance with the desired working principles and design goals, the spectrometer should have a large field of view, wide spectrum, high precision, and light weight. To make the structure more compact, a push-broom linear array CMOS detector without moving parts is used as the imaging method. To make the weight lighter, a transmission optical system and a filter are used as the spectroscopic method.

The imaging spectrometer needs to use a telecentric optical path to achieve pupil matching between the front optical system and the subsequent imaging system. In addition to high imaging quality, the chromatic aberration of the system must be corrected accurately, with telecentric features on the image side, and the distortion value as small as possible. To achieve the above requirements, a detailed analysis and comparison of the possible system forms was carried out. A Double Gaussian objective is a commonly-used optical system that has a large aperture and a large field of view, but it is difficult to achieve tele centricity on the image side. Fisheye lenses can achieve very large FOVs, but distortion is difficult to eliminate. An anti-telephoto objective has a strong ability to eliminate distortion. With this objective, the field of view can be enlarged, it can be in front of the focus, and one can use a field lens to form an image telecentric. Therefore, after in-depth analysis and research, a complicated anti-telephoto type is selected for optical design, which we determined to the best choice to achieve a wide-angle and maintain good chromatic aberration performance. Our optimized global optical system is shown in Figure. 3.

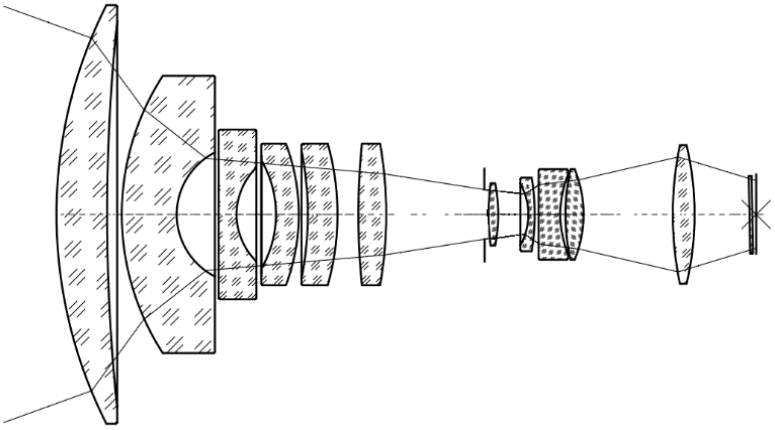

Figure 3. Optical design.

3.2. Structural Design

In accordance with our desired optical system parameters, the structure of the machine should have the following properties. First, it should provide precise positioning and support for optical lenses, diaphragms, and focal plane components. Second, the material should have a sufficient stiffness, with enough strength and resistance to deformation. Third, it should be lightweight and easy to adjust. Therefore, a modular design approach is adopted, according to the following:

1) The design of the opto-mechanical structure adopts the pressure ring method.
2) The material supplier chosen is a 7075 aluminum alloy.
3)Design lens barrel 1 module structure for assembling lens 1-6, design lens barrel 2 module for assembling aperture stop, lens 7-10 and field lens 11.
4) Design an electric box module to fix focal plane components and electronics.
5) Use an ultra-precision CNC machining method.
6) Use a support method with detachable connections, which consists of flanges, gaskets and screw threads.

The final optical-mechanical structure design shown in Figure. 4.

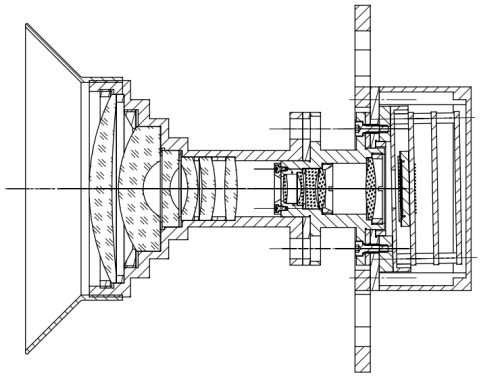

Figure 4. Optical-mechanical structure design.

4. Optimization and Analysis

4.1. Opto-mechanical Component Optimization

A topological optimization of the optical-mechanical components was performed in order to further reduce the volume of the structure. Using the thickness of the lens barrel and the position and thickness of the ribs as design variables, the solid isotropic material with penalization (SIMP) method was used for optimization [12], according to,

$$\begin{aligned} &\text{find}: \{x_1,...,x_n\} x_i = \begin{cases} 0 \\ 1 \end{cases} \quad i=1,...,n \\ &\min \quad C = F^T u \\ &\text{s.t} \sum_{i=1}^{n} V_i x_i \le \bar{V} \\ &F = ku \end{aligned} \tag{2}$$

The element density of each element is used as a design variable. After optimization, an element density of 1 or close to 1 indicates that the material is important and needs to be retained. An element density of 0 or close to 0 indicates that the element is not important and can be removed. This allows an achieve efficient use of materials, which can help achieve a lightweight but still effective design. The specific requirements are that the axial displacement of the lens barrel under the action of gravity load is $0.02\,mm$, and that the use of materials is optimized to minimize as much as possible. First, geometric editing, cleaning and simplified models are performed according to the initial design of lens barrel 1. Next, HyperMesh is used to develop a hexahedron model. Then, the mesh is divided and an element quality inspection is performed using the element quality inspection module to make the Jacobian ratio less than 0.7. The optimized finite element model is shown in Figure. 5.

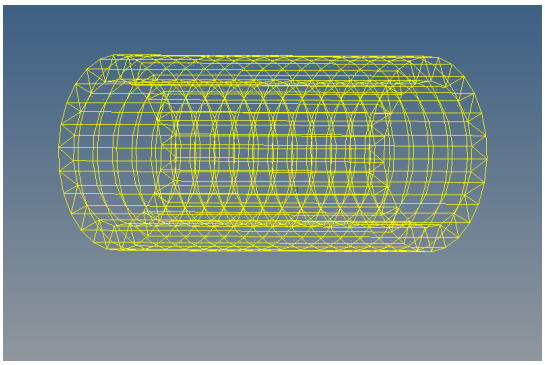

Figure 5. Finite element model to be optimized.

Components are created using 7075 aluminum alloy material, which has high strength, good corrosion resistance, an elastic modulus: $7.1\times10^4 MPa$, a Poisson's ratio of 0.33, and a density of $2.8\times10^{-9} t/mm^3$. The

support load set and airborne gravity load are used to guide the creation of components with the smallest volume and an optimized axial displacement of 0.02 *mm* as the response constraints. Optical-mechanical structure results are shown in Figure. 6.

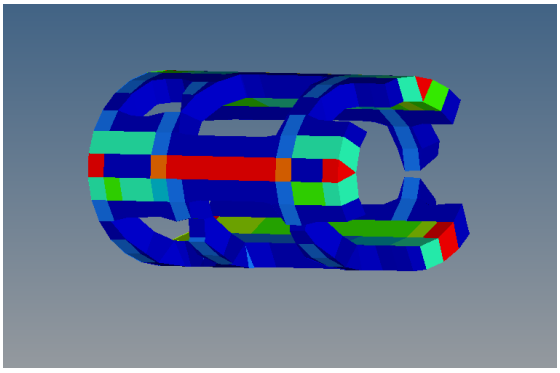

Figure 6. Topology optimization results.

Using the topology optimization results as a reference and taking into account the actual requirements of optical components, the advantages of 7075 aluminum alloy material structure compactness, and the cutting method, the hollow structure in Figure 6 was changed to a thin tube structure. In addition, a rib structure was added to the shell. These design results are shown in Figure 7.

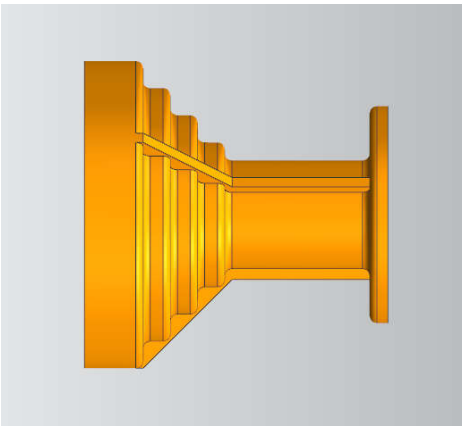

Figure 7. Actual design results.

4.2. Support Structure Optimization

The support structure was then optimized in order to further reduce the weight while still ensuring support strength. The SIMP method is again used for optimization in this step. The support structure model can be simplified into a two-dimensional model as shown in Figure. 8.

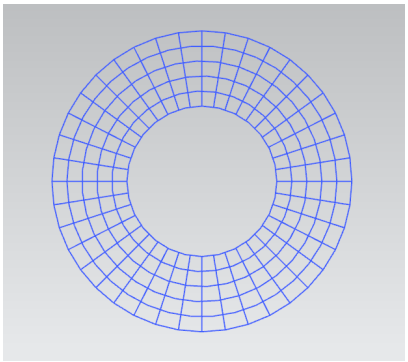

Figure 8. Two-dimensional geometric model of support structure.

The finite element model of the support structure is a geometric torus defined by an outer diameter r2 and an inner diameterr1. The model divides mi unit structures along the circumferential direction and nj unit structures along the radial direction. The geometric characteristics of the support structure make it difficult to divide into a uniform quadrilateral mesh, which will cause differences in the length and width of each unit. The calculation result of the element sensitivity is related to the length and width of the element, since the SIMP method uses the unit as the design variable. The length and width of different units will cause different removal orders in the optimization, so that the results of the optimization have unit dependence. Current solutions include element weighted sensitivity filtering and density slope control [13]. Our approach employs a mixed partitioning method of four-node units and three-node units. This method can make the geometric characteristics of the elements close to equal and avoid elements that are excessively long or too wide. The finite element division and support structure optimization model is shown in Figure 9.

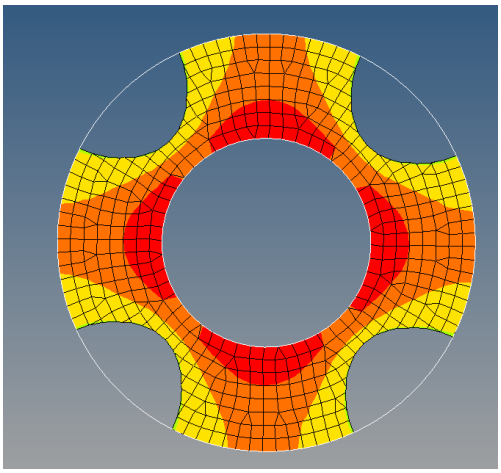

Figure 9. Optimization model of support structure.

Using the optimization result as a reference, the actual strength of the support, the structural characteristics of the material, the processing technology and the cost are considered. The result is a flange structure, and holes with are added to the flange surface to reduce weight. The design result is shown in Figure. 10.

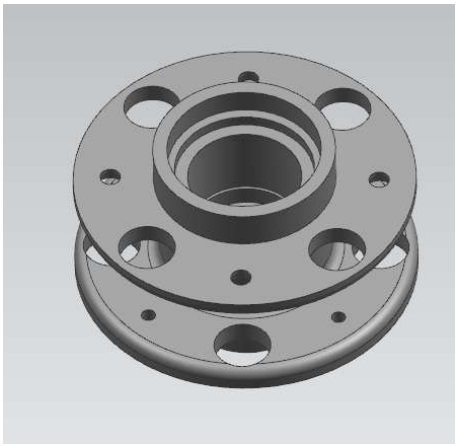

Figure 10. The actual design of the support structure.

4.3. Mechanical Analysis

Strength is a basic requirement that airborne optical instruments must meet. By solving the structure's response under load, the structure strength, stiffness performance and the amount of deformation of the optical lens can be obtained, and then the structure can be analyzed to meet the optical system accuracy requirements [14].

The equation of the structural demand solution under load is,

$$Ku = P \tag{3}$$

where K is the stiffness matrix of the optical-mechanical structure of the spectrometer, u is the

displacement vector, and P is the load vector acting on the optical-mechanical structure of the spectrometer. According to the finite element model of the structure, the corresponding materials, properties, loads, constraints and conditions are created. The stress intensity of the optical-mechanical structure is up to $1.17\times10^{5}\,Pa$, far less than the yield of the structure itself. The elastic modulus of the material used in the lens barrel is approximately $72\,GPa$, which provides adequate resistance to deformation.

Considering the deformation of the optical lens, we choose lens 2 to have a larger diameter, the largest attached load, and the largest amount of deformation as an example for analysis. The deformation cloud diagram of lens 2 is shown in Figure 11. Unlike other lenses in the structure, the center deformation amount of lens 2 is the largest and the edge deformation amount is the smallest, due to structural design reasons. The load direction is in the optical axis direction. Under the influence of a gravitational load, the maximum deformation of the center of lens 2 is $2.17\times10^{-8}m$, and the mean rigid body displacement is $1.2\times10^{-6}m$. The distortion of the other optical lenses exceeds the design goal.

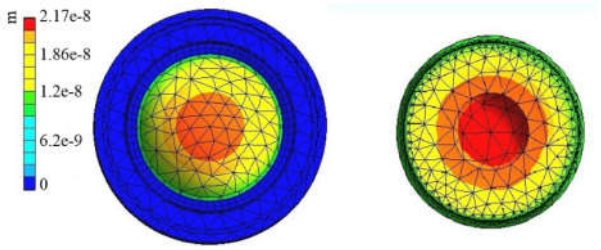

Figure 11. Lens 2 variant cloud map.

The vibrational conditions are also a very important consideration for drone design. Light drones will be more vulnerable to vibrations during flight. The most important is low frequency sinusoidal vibrations, with a frequency range of about 5~80 Hz. In order to evaluate the dynamic interaction of supporting components and supporting structures, guide experiments and calibration, an analysis of natural vibration characteristics is necessary. The vibrational frequency and mode are calculated by the following equation,

$$\left([K]-\omega_i^2[M]\right)\{\phi_i\}=0 \tag{4}$$

The frequency and mode shapes of the first 6 orders obtained by modal and vibrational analysis software are shown in Table. 1.

Table 1. The values of time in the mill drum first section

Order	Frequency (Hz)	Mode characteristics
1st	590.8	Vertical bend
2ed	598	Vertical bend
3rd	1307	Reverse
4th	1329.3	Reverse
5th	1330.4	-
6th	2056.7	-

The first-order modal frequency of the imaging spectrometer is 590.8 Hz, and the mode shape is characterized by vertical bending. Thus, the natural vibration frequency of imaging spectrometers is much higher than the normal vibration frequency range of light UAV flight (e.g., 5-80 Hz). Therefore, the imaging spectrometer will not resonate with a certain type of drone when it is working.

5. Environmental Adaptation Research

5.1. Aerodynamic Environmental Adaptation

When the drone is flying in the air, in addition to being affected by aerodynamic loads and causing shock and vibration, the instruments it carries may also be affected, since its. cruising speed is $100\,km/h$. Due to the size limitation in the cabin, the module of lens barrel 1 of the imaging spectrometer will partially extend out of the cabin, and the aerodynamic load and high-altitude wind speed will have an additive effect on the imaging spectrometer. Therefore, it is necessary to analyze the aerodynamics of the imaging spectrometer and study its aerodynamic adaptation. We conducted these analyses under the worst-case, scenarios, i.e., that lens barrel 1

would fully extend out of the cabin. For a freely flowing fluid with a ρ_∞ and a velocity v_∞, its dynamic pressure and pneumatic pressure, q_∞ are,

$$q_\infty = \frac{1}{2}\rho_\infty v_\infty^2 \tag{5}$$

Equation (5) shows the surface pressure distribution of aerodynamic objects. The aerodynamic force of the spectrometer can be decomposed into the resistance F parallel to the horizontal ground directions X, and Y, and the lift force N perpendicular to the ground in the vertical direction Z. The corresponding lift coefficient c_l and resistance coefficient c_d can be calculated by the formulae below,

$$\begin{aligned} c_n &= \frac{1}{c}\left[\int_0^c (C_{pl} + C_{pu})dx + \int_0^c (C_{fu}\frac{dy_n}{dx} - C_{fl}\frac{dy_l}{dx})dx\right] \\ c_a &= \frac{1}{c}\left[\int_0^c (C_{pu}\frac{dy_n}{dx} - C_{pl}\frac{dy_l}{dx})dx + \int_0^c (C_{fu} + C_{fl})dx\right] \\ c_l &= c_n\cos\alpha - c_a\sin\alpha \\ c_d &= c_n\sin\alpha + c_a\cos\alpha \end{aligned} \tag{6}$$

We use an iterative method to import the model as the solution parameter and use Hyper software to perform the iterative solution. From the plots of solution vs iteration number shown in Figure 12, we can see that the solution tends to converge for more than 200 iterations, giving an approximation for the lift coefficient c_l and the drag coefficient c_d.

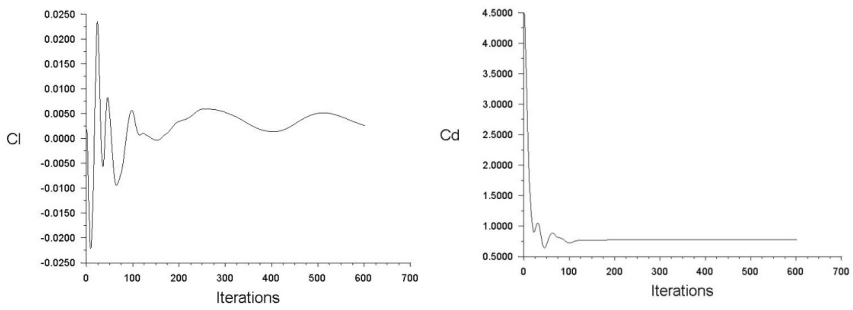

Figure 12. The iterative solution of lift coefficient and drag coefficient.

In cruise mode, the lift coefficient c_l of the spectrometer is approximately 0.01, and the lift force N of the spectrometer can be ignored. The resistance coefficient c_d of the spectrometer is approximately 0.3, so the influence of the resistance needs to be considered in the analysis. Aerodynamic software is used for simulation experiments, and the aerodynamic pressure and aerodynamic streamlines around the spectrometer are obtained as shown in Figure. 13.

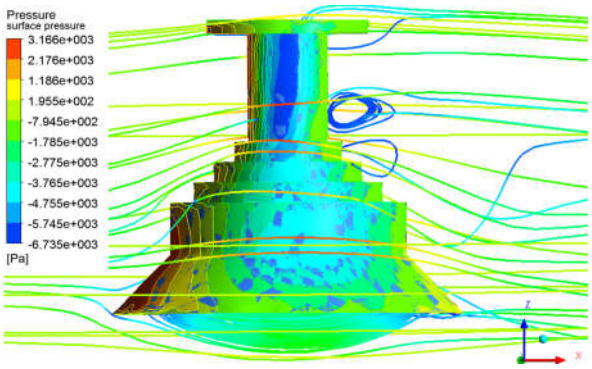

Figure 13. Aerodynamic flow diagram around the spectrometer.

The results of the simulation calculation and simulation analysis under the condition of a 100 km/h cruising speed of 100 km/h and a wind level of 7 (50-61 km/h) show that the maximum deformation of the spectrometer lens does not exceed 0.002 mm.

5.2. Temperature Environmental Adaptation

The outside temperature is generally relatively constant when the drone is at cruising speed. However, in special cases, such as when the drone passes through clouds, the ambient temperature may change greatly. For example, when a drone is driving into a cumulonimbus cloud layer during summer in the Northern Hemisphere, the ambient temperature can drop to about 0 $℃$ due to the large amount of water droplets and ice particles in the cloud layer. When exposed to a strong radiation effects, the ambient temperature can rise sharply to about 40 $℃$. Rapid changes in temperature can cause mechanical structures and optical lenses to deform. Therefore, a thermodynamic analysis is performed on the imaging spectrometer to study whether its temperature adaptation range meets the requirements of the index. The process temperature adaptation follows the first law of thermodynamics. For a closed system,

$$Q - W = \Delta U + \Delta KE + \Delta PE \tag{7}$$

Where Q is the heat, W is the work done by the system, ΔU is the internal energy of the system, ΔKE is the kinetic energy of the system, and ΔPE is the potential energy of the system. For the case of environmental temperature adaptation of the imaging spectrometer, the inflow heat of the system plus the heat generated by the system itself is equal to the heat flowing out of the system.

$$\left[K(T)\right]\{T\} = \{Q(T)\} \tag{8}$$

Where $\left[K(T)\right]$ is the conduction matrix, $\{T\}$ is the node temperature vector, and $\{Q(T)\}$ is the node heat flow rate vector. The geometric parameters and the thermal performance parameters of the material and the boundary conditions are used to solve the energy balance equation.

Thermodynamic software was used for simulation analysis. The spectrometer shape was used as the geometric parameter, aluminum alloy was used as the material parameter, and external heat flow was used as a boundary condition of the second type. The axial deformation of lens 1 can be obtained with a standard temperature of 22 $℃$ and a temperature range of 0-40 $℃$, as shown in Figure 14.

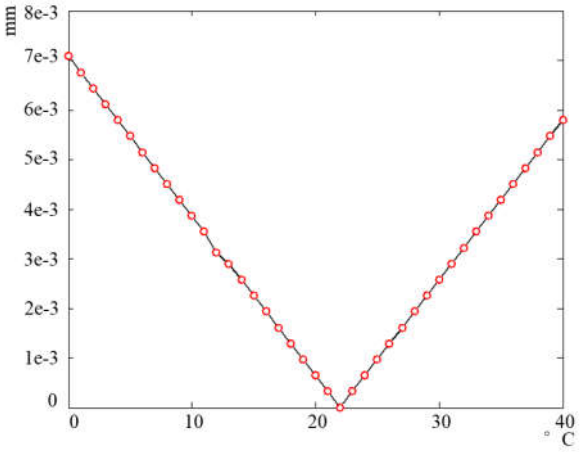

Figure 14. Lens deformation at ambient temperature of 0-40 $℃$.

In the range of 0-22 $℃$, the amount of deformation will decrease linearly as the temperature rises, and in the range of 22-40 $℃$, the amount of deformation will increase linearly as the temperature rises. Within the range of 0-40 $℃$, the deformation amount of lens 1 does not exceed the 0.01 mm level required by the optical design tolerance. Thus, our design can easily adapt to the expected temperature changes.

6. Experimental Testing

After the results of our design, analysis, and environmental adaptation research, the system was mapped, processed, and adjusted. The structure, volume and weight of the spectrometer are consistent with the design values; the size is $175 \times 175 \times 175\,mm$, and the optical machine structure weight is $1.15\,kg$. The optical lens processing accuracy, installation and adjustment errors are in line with the expected design goals.

We performed interferometer surface accuracy monitoring and field simulation experiments in order to accurately adjust the focal plane. The surface accuracy of the RMS center field of view is 0.016 and the edge field of view RMS is 0.023, which meets the expected design goals. For outdoor experiments, a building at a distance of approximately $1\,km$ can be selected, and a target of $0.5\,m$ can be resolved, which is close to the

design index. The outdoor experiment is shown in Figure 15.

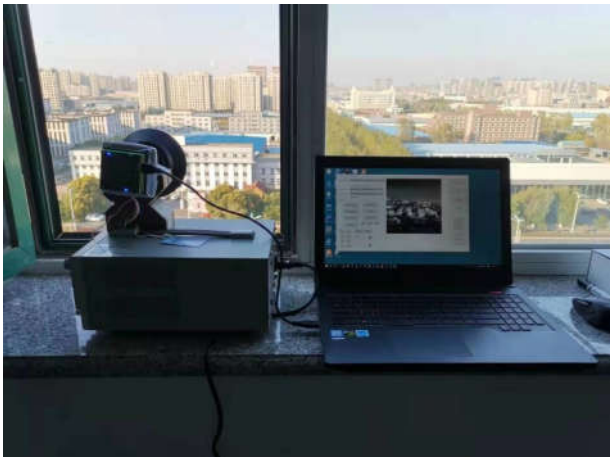

Figure 15. Outdoor experiment design setup.

In order to better focus the plane, a laboratory focus experiment is performed. The laboratory fixed-focus experiment platform consisting of a light source, a calibration plate, a collimator, a spectrometer, and a DC power supply. Four edge field-of-view points were selected for adjustment. After testing, the field-of-view angle was 60.2°, which was within tolerance of the design requirement of a field-of-view angle of 60 . The results of the fixed-focus experiment are shown in Figure. 16.

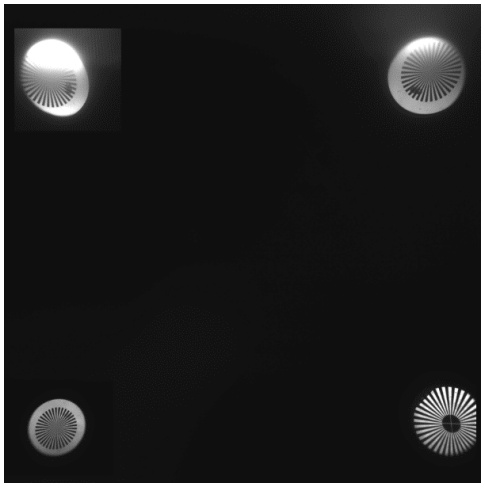

Figure 16. Results of fixed focus experiment

7. Conclusions

With the advancement in networking and multimedia technologies enables the distribution and sharing of multimedia content widely. In the meantime, piracy becomes increasingly rampant as the customers can easily duplicate and redistribute the received multimedia content to a large audience.

This paper has detailed the development of a light unmanned airborne imaging spectrometer. The optical system, overall structure, and sub-system structures are designed based on the principles and methods of filter beam splitting, push-broom imaging, and modular design. Its size is $175 \times 175 \times 175\ mm$ and its optical-mechanical structure weight is $1.15\ kg$. Finite element theory is used to calculate and analyze the linear static structure and natural vibrational characteristics. The strength of the optical-mechanical structure and the deformation of the optical exceed the technical requirements. The first-order modal frequency is $590.8\ Hz$, and the natural vibrational characteristics are adequate. The environmental adaptability of the imaging spectrometer was also analyzed. In the temperature range of $0 \sim 40\ ^{\circ}C$ with wind conditions less than or equal to 7 and a cruising speed of $100\ km/h$, the drone can still perform well. The design, analysis, research and experiments done in this paper can provide theoretical support and technical guidance for future design and optimization efforts of light airborne spectrometers, information acquisition experiments and collaborative networking.

Acknowledgements

This work was supported by Chinese Academy of Sciences Strategic Pilot Project No. XDA17040201 and National key R & D plan No. 2017YFB0503001.

References

[1] Wang, Q., Li, Y., & Liu, X. (2018) "Analysis of Feature Fatigue Eeg Signals Based on Wavelet Entropy", *International Journal of Pattern Recognition and Artificial Intelligence*, 26(11), pp. 2675-2683.
[2] Cao, T. S., Shi, Z. H., LIN, G. Y. (2017) "Develop of Airborne Ocean Modified Dyson Hyperspectral Imager", *Optics and Precision Engineering*, 25(06), pp.1403-1409.
[3] Gregg, V., and, Robert, O. (1993) "The Airborne Visible/Infrared Imaging Spectrometer (Aviris)", *Remote Sensing of Environment*, 44(2), pp.127-143.
[4] Kruse, F. A., Boardman, J. W., Lefkoff, A. B. (2000) "Hy Map: An Australian Hyperspectral Sensor Solving Global Problems-Results from USA Hy Map Data Acquisitions", *Proc. of the 10th Australasian Remote Sensing and Photogrammetry Conference*, pp.18-23.
[5] Anna, M. M., Roman, D. "Hybrid Energy Systems in Unmanned Aerial Vehicles", *Aircraft Engineering and Aerospace Technology*, 91(5).
[6] Haris, K., Sofiane, M., Benjamin, M., Jean-Baptiste, T., & Jon, H. (2018). "Hytexila: High Resolution Visible and Near Infrared Hyperspectral Texture Images", *Sensors,* 18(7), pp.2045-2049.
[7] Tristan, P., Touria, B. (2017) "Hyperspectral remote sensing of coral reefs by semi-analytical model inversion – comparison of different inversion setups", *Remote Sensing of Environment*. 190, pp.348-365.
[8] Cong-Jun, W. U., & Chang-Xiang, Y. (2012) "Imaging Spectrometer Optical Design Based on Prism-Grating-Prism Dispersing Device", *Journal of Applied Optics, 33*(1), pp.37-43..
[9] Luo, G. Y., WANG, B. T. (2017) "Design of Visible Near Infrared Imaging Spectrometer on Unmanned Aerial Vehide", *Acta Photonica Sinica*, 46(9).
[10] Gao, Z. L. (2014) "Design of Hyperspectral Imager Equivalent Focal Plane Assembling Module", *Chinese Optics*, 7(04), pp.644-650.
[11] Huang, M., Xiang, L. B. (2010) "Research on Spatially Modulated Fourier Transform Imaging Spectrometer Data Processing Method", *Spectroscopy and Spectral Analysis*. 30(03), pp.855-858.
[12] Bonyan, H. Khamseh, S. Ghorbani, F. Janabi-Sharifi. (2019) "Unscented Kalman Filter State Estimation for Manipulating Unmanned Aerial Vehicles", *Aerospace Science and Technology*, 92.
[13] Ciani, G., Arain, M. A., Aston, S. M., Feldbaum, D., Fulda, P., & Gleason, J. (2016) "Small Optic Suspensions for Advanced Ligo Input Optics and other Precision Optical Experiments", *Review of Scientific Instruments, 87*(11), pp.114504.
[14] Emeis, S. (2014) "Wind Speed and Shear Associated with Low-Level Jets over Northern Germany", *Meteorologische Zeitschrift,23*(3), pp.295-304.